Ni-Based Electrocatalysts for Unconventional CO_2 Reduction Reaction to Formic Acid

Enrico Lepre,[a] Julian Heske,[a,b] Michal Nowakowski,[c] Ernesto Scoppola,[a] Ivo Zizak,[d] Tobias Heil,[a] Thomas D. Kühne,[b] Markus Antonietti,[a] Nieves López-Salas[a] and Josep Albero*[a]*

a. Max Planck Institute of Colloids and Interfaces, Research Campus Golm, D-14424 Potsdam, Germany; University of Potsdam, D-14424 Potsdam, Germany.
b. Dynamics of Condensed Matter and Center for Sustainable Systems Design, Chair of Theoretical Chemistry, University of Paderborn, Warburger Str. 100, D-33098 Paderborn, Germany.
c. Department of Chemistry and Center for Sustainable Systems Design, Paderborn University, Warburger Strasse 100, Paderborn 33098, Germany
d. Helmholtz-Zentrum Berlin für Materialien und Energie, Albert-Einstein-Str. 15, 12489 Berlin, Germany
* e-mail: nieves.lopezsalas@mpikg.mpg.de, josep.albero@mpikg.mpg.de

Keywords: CO_2 reduction reaction, noble carbon, Ni-O4 electrocatalysts, formic acid

Abstract

Electrochemical reduction stands as an alternative to revalorize CO_2. Among the different alternatives, Ni single atoms supported on carbonaceous materials are an appealing catalytic solution due to the low cost and versatility of the support and the optimal usage of Ni and its predicted selectivity and efficiency (ca. 100% towards CO). Herein, we have used noble carbonaceous support derived from cytosine to load Ni subnanometric sites. The large heteroatom content of the support allows the stabilization of up to 11 wt% of Ni without the formation of nanoparticles through a simple impregnation plus calcination approach, where nickel promotes the stabilization of C_3NO_x frameworks and the oxidative support promotes a high oxidation state of nickel. EXAFS analysis points at nickel single atoms or subnanometric clusters coordinated by oxygen in the material surface. Unlike the well-known N-coordinated Ni single sites selectivity towards CO_2 reduction, O-coordinated-Ni single sites (ca. 7wt% of Ni) reduced CO_2 to CO, but subnanometric clusters (11 wt% of Ni) foster the unprecedented formation of HCOOH with 27% Faradaic efficiency at -1.4V. Larger Ni amounts ended up on the formation of NiO nanoparticles and almost 100% selectivity towards hydrogen evolution.

1. Introduction

Electrochemical conversion of CO_2 into chemicals or fuels using renewable electricity has been demonstrated as a very promising strategy for not only mitigating climate change but also producing high value-added chemicals. However, the development of efficient, selective, and stable catalysts is considered the main drawback to implement this technology in practical applications.[1-4] Among the different candidates, transition metal-based catalysts supported on carbonaceous materials have attracted increasing attention due to their good electrocatalytic performance, versatility, and economic advantages of using abundant raw materials.[5, 6]

Different strategies for efficient, selective, and stable catalysts preparation have been carried out recently, including surface modification, heterojunctions formation, tailoring metal crystal facets, or the number of defects, among others.[7-9] The size of the supported metal nanoparticles has been identified to play a key role in the activity and selectivity of heterogeneous catalysts.[10] In general terms, the activity of metal nanoparticles increases when their size decreases, and hence, sub-nanometric scale size reduction down to dozens or even single atoms can give rise to striking properties.[11, 12] For instance, Strasser and co-workers studied the influence of Cu nanoparticle sizes on the electrochemical CO_2 reduction reaction (CO_2RR) activity and selectivity. The smallest Cu nanoparticles at 2 nm and below showed the highest electrocatalytic activity due to the high ratio of low-coordinated surface atoms towards bulk atoms. However, the formation of hydrocarbons (CH_4, C_2H_4) was predominant at large Cu nanoparticles (> 15 nm), while nanoparticles of 2 nm or below showed high CO selectivity.[13] Similarly, Huan et al. reported the size-dependent selectivity of Fe decorated carbon catalysts for the CO_2RR. While Fe single sites could reduce CO_2 to CO, larger nanoparticles would preferentially reduce water to hydrogen (i.e., hydrogen evolution reaction, HER).[14]

The limiting factor for developing catalysts utilizing metal sites in the subnanometer scale is the stabilization of metallic atoms or clusters on the support surface.[15] Strong metal-support

grafting is required to avoid agglomeration of the metal atoms into larger (nano)particles. Heteroatom-doped carbonaceous materials have recently been demonstrated to be very convenient supports with the potential to overcome this issue in electrocatalysis.[16] Heteroatoms allocated in a carbon matrix can alter their electronic properties (i.e., adding or removing charge density), favouring the interaction with some metals. In this context, doped noble-carbonaceous materials have recently found much attention as viable support due to their high and predicted structurally ordered heteroatom content.[17] The nobility of these materials provides high stability against oxidation or combustion. Doped noble-carbonaceous materials have demonstrated high CO_2 adsorption, large specific surface area, and proper electrical conductivity.[17-20]

Theoretical studies predicted that highly nitrogen-doped carbonaceous networks could stabilize transition metal atoms and ions towards different reactions.[19, 21, 22] Remarkably, Ni was identified as a champion candidate for the CO_2RR due to its enhanced activity towards CO when the metals were anchored on N-doped carbonaceous supports.[23] Recent reports show that the coordination environment of nickel also deeply affects its electrochemical selectivity. For instance, Ni single sites coordinated to four nitrogen atoms are known to be electroactive for the oxygen reduction reaction (ORR).[24, 25] However, Song et al. reported in early 2020 that oxygen coordinated Ni decorated on top of graphene turned out to be highly selective and efficient towards H_2O_2 when used as electrocatalyst for ORR.[26] Soon after, Wang et al. reported that Ni on carbon supports comprising N_2O_2 environments (i.e., intermediate coordination sphere between Ni-N_4/C and Ni-O_4/C) were also highly selective towards H_2O_2.[27] The potentials at which ORR and CO_2RR are occurring are very different, and one first and reasonable thought is that the reduction potential at which the CO_2RR occurs might comprise the stability of metal oxide-derived electrocatalysts. In this context, in 2017, Pander III et al. published a review trying to unveil the performance of metal oxide-derived catalysts for the CO_2 reduction reaction.[28] Reports, which show that stable Sn oxide-derived materials

(with kinetic stability far exceeding the predicted thermodynamic stability of the materials) and metallic tin have very different formate yields, are indeed in line with the observations of Wang and Song for ORR. However, to the extent of our knowledge, no study reports on the use of Ni-O_4 single sites decorated carbons or the effect of the size changes in the performance of the materials as electrocatalysts for the CO_2RR.

In this work, a facile, multi-gram approach to synthesize nickel-decorated electrocatalysts comprising Ni atoms anchored through oxygen sites to highly doped nitrogen supports is developed and the effect of the sites in their performance as CO_2RR is studied. To do so, we have prepared a doped, noble-carbonaceous material as support using cytosine as an organic precursor and an inorganic salt melt (1:1 wt% of NaCl and $ZnCl_2$) as porogen. The large surface area, nitrogen content, and oxidation resistance of the material allowed preparing a set of Ni-decorated catalysts with different Ni loadings: A simple route using impregnation with a metal-organic nickel precursor plus subsequent calcination is employed. The materials have been fully characterized, and their performance as catalysts for the CO_2RR is evaluated and correlated with the physicochemical properties of the samples as well as the chemical environment and site size of the nickel on their surface.

2. Results and discussion

A cytosine-derived carbonaceous material comprising a C/N ratio of 5.7 (77 wt% of carbon and 16 wt% of nitrogen according to EDX analysis) was prepared as prior reported by our group.[29] In brief, cytosine was mixed and grinded with a mixture of salt melts composed of 1:1 wt% NaCl and $ZnCl_2$ that acted as porogen. The mixture was submitted to carbonization at 800°C under N_2 atmosphere and washed in HCl several times after cooling down. The carbon powder obtained will be referred to hereafter as NC (see **Scheme 1s**). NC showed outstanding thermal stability in air with no significant mass loss during heating up to 600°C, as shown by thermogravimetric analysis in air atmosphere (**Figure S1**).

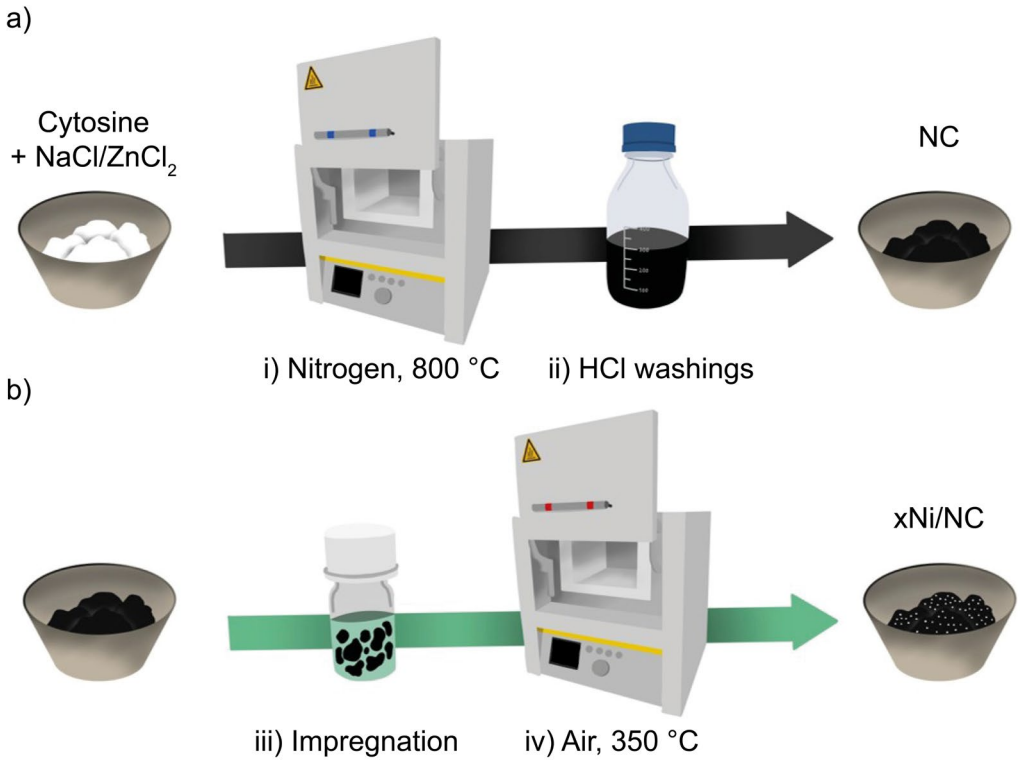

Scheme 1. Ni-decorated NC preparation procedure. Preparation includes: (i) cytosine and melting salts mixtures are submitted to heat treatment, (ii) powder washing and drying. The final $_X$Ni/NC materials are obtained through (iii) NC dispersion in solutions with different $Ni(acac)_2$ content and (iv) calcination of the obtained dry powder.

The sample morphology, the large heteroatom content, and the oxidative resistance of NC make it a great candidate as support for transition metal single atoms. Samples containing different Ni loadings were prepared in multigram scale and high yields (**Table 1**), following the synthetic procedure described in the Experimental Section. In brief, different amounts of $Ni(acac)_2$ were deposited on NC through a wet impregnation method. The Ni-impregnated NC dry powders were calcined at 350°C in air rendering the final $_X$Ni/NC samples. **Scheme 1b** shows the preparation procedure. ICP-OES was used to determine the final Ni loading in the C800Nix samples. The results indicate that the increasing amounts of $Ni(acac)_2$ evolve in a gradual Ni loading enhancement of $_X$Ni/NC samples, being of 0, 2, 4, 11, and 33 wt% for NC, 2Ni/NC, 6Ni/NC, 10Ni/NC, and 30Ni/NC, respectively.

The XRD pattern of NC showed a peak with low intensity at 26.5°, attributed to graphitic π-π stacking (**Figure S2** in Supplementary Information).[29] This weak signal indicates that the

graphitic layers were not stacked as already observed in the previous salt melt synthetic approaches.[30, 31] Interestingly, the addition of Ni does not promote graphitization as previously reported,[32-34] and the graphitic stacking peak remains broad and weak (**Figure S2**). On the other hand, crystalline peaks related to Ni, NiO, or NiOH were not detected in 2Ni/NC, 6Ni/NC, or 10Ni/NC samples. On the contrary, 30Ni/NC presents three broad peaks centred at 38°, 43°, and 63°, which are characteristic of NiO. Using the Scherrer equation, the NiO main crystal size in 30Ni/NC was determined to be about 5 nm. It is well known that very smaller nanoparticles (< 5 nm) can be invisible for this technique.[35]

Table 1. Summary of the composition of materials according to EDX analysis and ICP-OES and data extracted from N_2 and CO_2 isotherms at 77K and 273K, respectively.

	Yield	EDX elemental analysis (wt%) [a]					C/N	S_{BET} [b]	V_T [c]	V_{mic} [d]
Sample	**%**	**C**	**N**	**O**	**Zn**	**Ni**	**At.**	**(m^2/g)**	**(cm^3/g)**	**(cm^3/g)**
NC	-	77	16	6	0.4	-	5.7	1820	1.30	0.25
2Ni/NC	79	76	13	6	0.6	2 (2)	7.0	1771	1.16	0.22
6Ni/NC	82	75	13	7	0.5	7 (4)	6.9	1843	0.99	0.20
10Ni/NC	80	54	16	15	0.9	12 (11)	3.9	1017	0.55	0.20
30Ni/NC	-	35	9.4	17.2	2.9	30 (33)	4.5	40	0.11	0.03

[a] Ni ICP-OES data are given in brackets for comparison purposes; [b] Specific surface area was calculated using the Brunauer–Emmett–Teller equation; [c] total pore volume (V_T) was caluculated at P/P_0=0.995; [d] microporous volume (Vmic) was calculated from CO_2 adsorption isotherms using a DFT model.

SEM images of the different samples confirm that the morphology of the NC support suffers negligible changes upon Ni loading (**Figure S3** in Supplementary Information).[29] EDX analysis of the $_X$Ni/NC samples confirmed the presence of Ni in all samples, and a gradual Ni content increase with the $Ni(acac)_2$ loading, which is in good agreement with the ICP-OES results (see **Table 1**). The CNO composition of the surface of the materials was also determined using EDX analysis. The standard deviation of our CNO analysis is ca. ± 2 for all three elements. Thus, samples NC, 2Ni/NC and 6Ni/NC are virtually the same in CNO composition (see **Table 1**). As for sample 10Ni/NC, the amount of nickel loaded starts changing the CNO composition on the surface of the material. The change is more dramatic for 30Ni/NC that has a much different CNO composition than that of the other samples (see **Table 1**). The analysis show that

the oxygen conten important increase in the oxygen content of the outer shell of these materials. Here, it is important to remember that nanoparticles were detected in 30Ni/NC by XRD. Thus, it is plausible that subnanometric clusters are also presence in 10Ni/NC. The Zn content in the samples is reminiscent of the salt melt used for the preparation of NC. The standard deviation of the measurement of Zn using EDX analysis is ± 0.1. Thus, the amount of Zn does not significantly change for samples NC, 2Ni/NC, 6Ni/NC, and 10Ni/NC (**Table 1**). The increase of Zn content observed for this sample is most likely due to the formation of non-volatile ZnO during the impregnation process while most of the carbon might be released through the formation of carbonaceous volatile compounds.

TEM images show that NiO nanoparticles with an average diameter of 5.1 ± 1.7 nm, after measurement of a statistically relevant number of samples, can only be observed in the 30Ni/NC (**Figure S3**), which is in good agreement with calculations using the Scherrer equation applied to XRD data. Nanoparticles were not observed in the other $_X$Ni/NC samples, indicating that nickel could be incorporated on the NC substrate as single atoms or forming small clusters in the sub-nanometer range.

Dark field and bright field STEM images of $_X$Ni/NC help to elucidate how Ni was incorporated in the 2Ni/NC, 6Ni/NC, and 10Ni/NC samples (**Figure 1**). The images show subnanometric particles homogeneously distributed on top of NC. Many factors influence the STEM intensity at this magnification scale, which makes it hard to draw reliable conclusions. But in general, the observed sites appear with an average size of about 0.25 nm. Moreover, site density was found to be 1.40 nm^{-2}, 2.09 nm^{-2}, and 2.55 nm^{-2} for 2Ni/NC, 6Ni/NC, and 10Ni/NC, respectively. These results point at 2Ni/NC, 6Ni/NC, and 10Ni/NC samples having different amounts of Ni subnanometric sites homogeneously distributed on top of the NC substrate, but the formation of small clusters cannot be discarded.

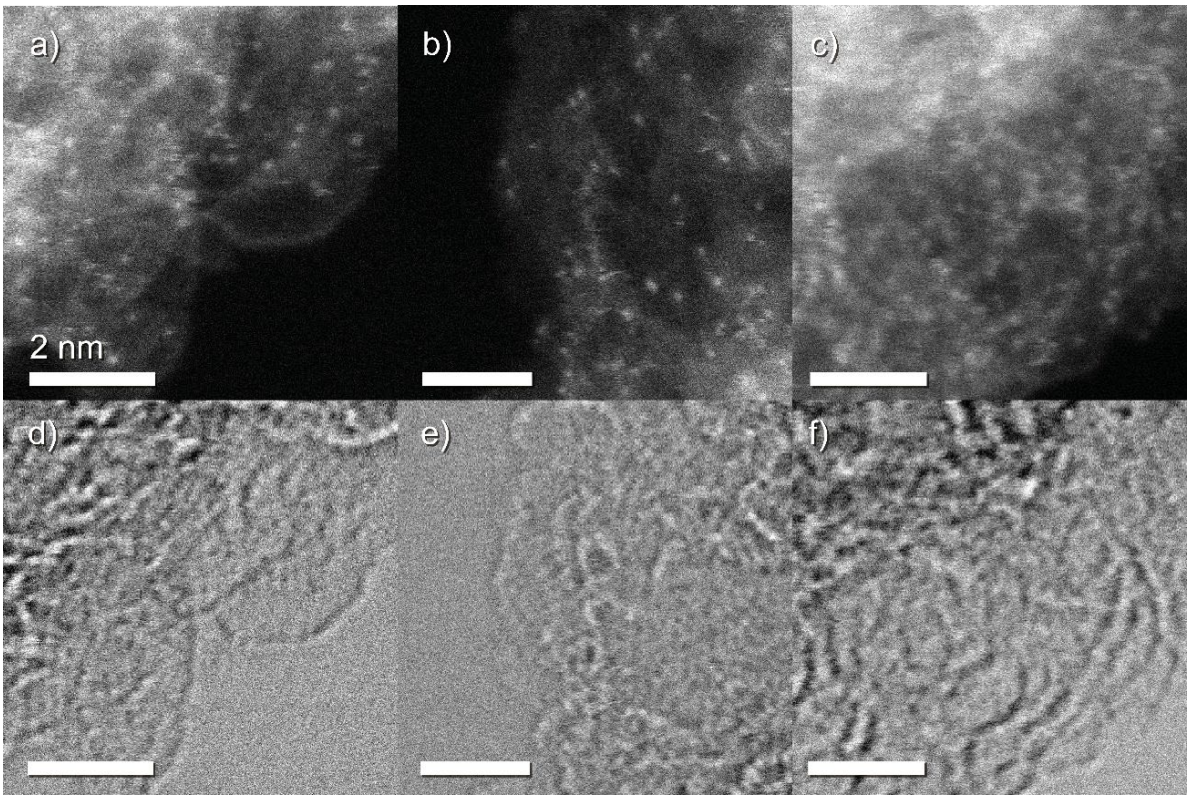

Figure 1. STEM dark field (top panel) and bright field (bottom panel) mode micrographs of (a and d) 2Ni/NC, (b and e) 6Ni/NC, and (c and f) 10Ni/NC.

High-resolution XPS C1s spectra of **$_X$Ni/NC** samples and the best deconvolution to individual components did not evidence significant changes between samples (**Figure S4** in Supplementary Information). In all cases, the samples showed a main signal corresponding to C=C bonds at 284.6 eV and C-N, C=O, and -C=O bonds from adventitious compounds centred at 285.9 eV, 287.8 eV, and 290.4 eV, respectively. It is worth noting that no evidence of C-Ni bonds corresponding to $Ni_{1-x}C_x$ species at approximately 283.4 eV was found.[34] Similarly, deconvolution of N1s high-resolution XPS profiles of $_X$Ni/NC samples did not show significant differences between the samples, except 30Ni/NC (**Figure S4**). The $_X$Ni/NC N1s XPS signals were deconvoluted in different components corresponding to pyridinic-N (~ 397.9 eV), pyrrolic-N (~ 399.6 eV), quaternary-N (~ 401.3 eV), oxide-N (~ 403.4 eV), and the π-π* satellite (~ 405.6 eV). It is worth noticing that the pyrrolic-N component could overlap with the metal-N component. Nevertheless, no dramatic change has been observed in this region upon Ni content increase, suggesting that there is not a strong interaction between Ni and N. In the

case of 30Ni/NC, these components were also identified; however, the relative contribution of quaternary-N and N-oxides was lower than in the other cases, while the contribution of pyridinic-N increased. **Table S1** summarizes the contribution of each type of bond from C1s and N1s signals.

The high-resolution XPS Ni $2p_{3/2}$ spectra of the $_X$Ni/NC samples display the main peak composed of two components and the corresponding satellite. It can be observed that the relative contribution of these two components varies with the Ni content, and their position (see **Table S2**). The presence of Ni metal can be disregarded in all cases, since the typical component centered at 852.6 eV has not been detected in any sample. The XPS spectrum of 2Ni/NC shows the main component centered at approximately 854.8 eV. This binding energy has been previously reported in tetra carbonyl Ni complexes-like coordination,[36] while the second component, centered at 856.1 eV, can be attributed to Ni acetylacetonate complexes,[37] indicating overall diversified forms of oxygen coordinated to Ni. The increase in Ni content in 6Ni/NC and 10Ni/NC produces a shift in the individual components of the Ni $2p_{3/2}$ signal towards higher binding energies. For instance, the main component is shifted to 855.2 and 855.3 eV for 6Ni/NC and 10Ni/NC, respectively. Similarly, the component related to Ni $(acac)_2$ is shifted to 857.05 and 857.4 eV in 6Ni/NC and 10Ni/NC, respectively. These binding energies, higher than that of Ni(II), can be attributed to Ni species with a higher valence state (Ni(III)) or the changes in Ni(II) cluster size.[38, 39] Additionally, the contribution of the second component decreases with the growing Ni content, as can be seen in **Figure 2 a-c**. Finally, a very different XPS Ni $2p_{3/2}$ spectrum can be observed from the 30Ni/NC sample (**Figure 2 d**), where two main components at 855.8 and 853.95 eV, attributed to Ni(OH) and NiO, respectively, have been identified. It is worth noticing that XRD has previously anticipated the presence of NiO nanoparticles. However, due to the superficial character of the XPS, the

presence of a thin Ni(OH) layer in the outermost part of the NiO nanoparticles cannot be discarded.

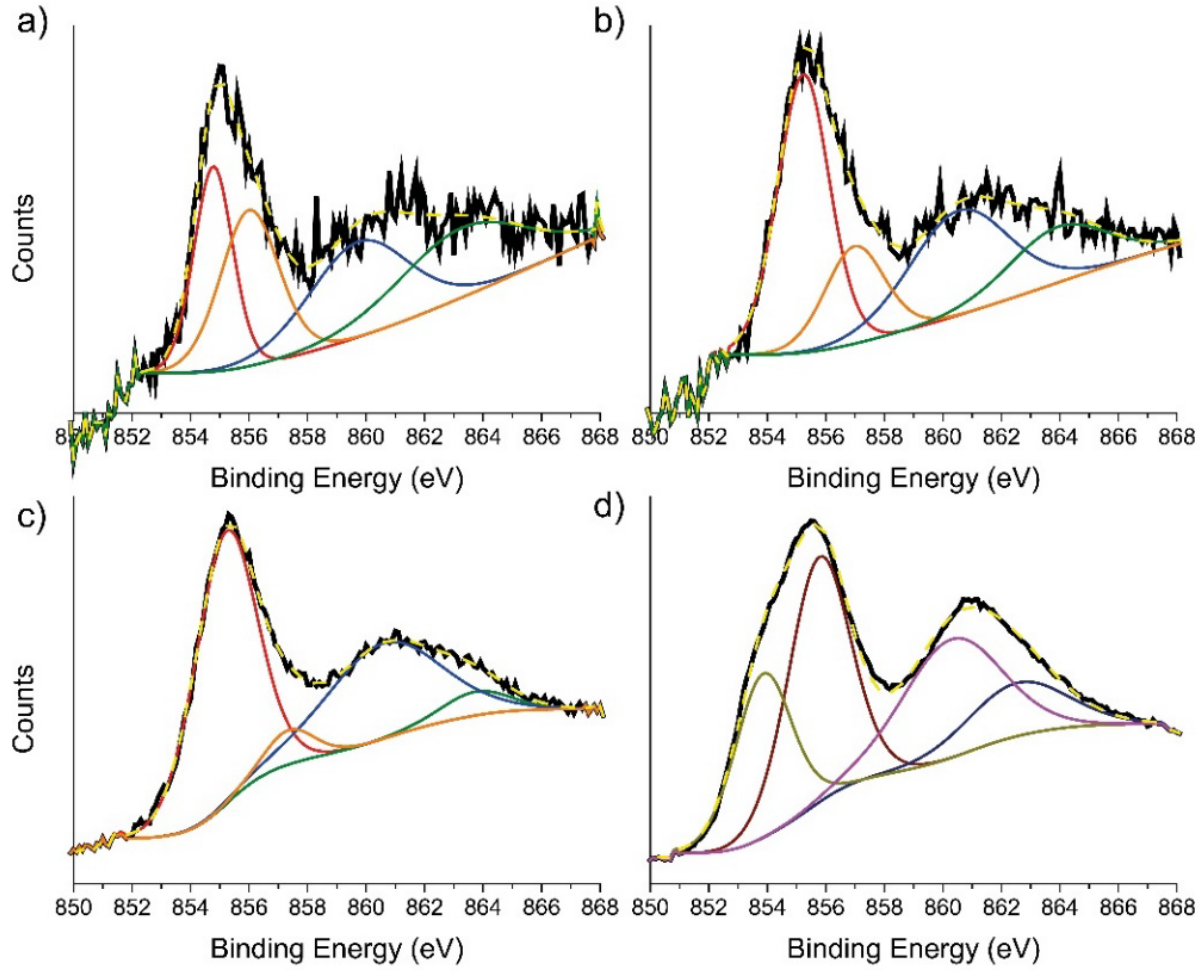

Figure 2. High-resolution XPS Ni $2p_{3/2}$ spectra and their best deconvolution to individual components of (a) 2Ni/NC, (b) 6Ni/NC, (c) 10Ni/NC and (d) 30Ni/NC.

In order to further study the presence of Ni single-atoms in the $_X$Ni/NC samples and the local structure of the Ni centres, Ni K-edge X-ray absorption near edge structure (XANES) and extended X-ray absorption fine structure (EXAFS) spectroscopy were performed.[40, 41], [42] **Figure 3a** shows the Ni K-edge XANES spectra for 2Ni/NC, 6Ni/NC, 10Ni/NC, and 30Ni/NC, along with the reference spectra of bulk metal Ni, NiO, and Ni acetylacetonate ($Ni(acac)_2$). The absorption edge energy of the Ni-containing samples is larger than that of the metal Ni (8333.0 eV) and NiO (8340.5 eV) references, but similar to those of $Ni(acac)_2$ (8350.0 eV). The shape of the XANES spectra of 2Ni/NC, 6Ni/NC, and 10Ni/NC and $Ni(acac)_2$ are very similar. This

is a first indication that all samples share a similar (average) coordination environment of the Ni centres. The high intensity of the white line (8353.5 eV) indicates a minimal sample thickness and a small self-absorption effect. Although the relation intensity-thickness for Ni nanoparticles was already reported,[43] the samples contain mixed-valence Ni compounds. Thus, the peak intensity may also be related to the average coordination number, for example, due to phase transition from fcc to hcp with growing cluster size.[44] XANES spectra of samples 2Ni/NC, 6Ni/NC, 10Ni/NC, and 30Ni/NC are progressively changing with the growing content of the initial $Ni(acac)_2$. The trend was further confirmed with the linear combination fitting (LCF) analysis (**Figure 3b**), where $Ni(acac)_2$, NiO, and Ni(0) were used as references. According to the fit results, the XANES spectrum of 30Ni/NC can be reproduced by 76.8(4.7) % of isolated, oxygen-coordinated $Ni(acac)_2$, 22.1(2.9) % NiO and a minor fraction of 1.1(5.5) % bulk Ni^0. The amount of Ni^0 present in all samples is much lower than the nickel centers having a coordination environment similar to $Ni(acac)_2$ or that of NiO. Moreover, the standard deviation of the obtained values is always larger than the mean value obtained and thus the contribution of Ni^0 single atoms in the samples will be disregarded. The number of isolated, oxygen coordinated Ni is increasing with decreasing Ni loading to a maximum fraction of 99.9(3.4) %, while the fraction of bulk Ni shows the opposite trend, and for 2Ni/NC no Ni^0 is detected.

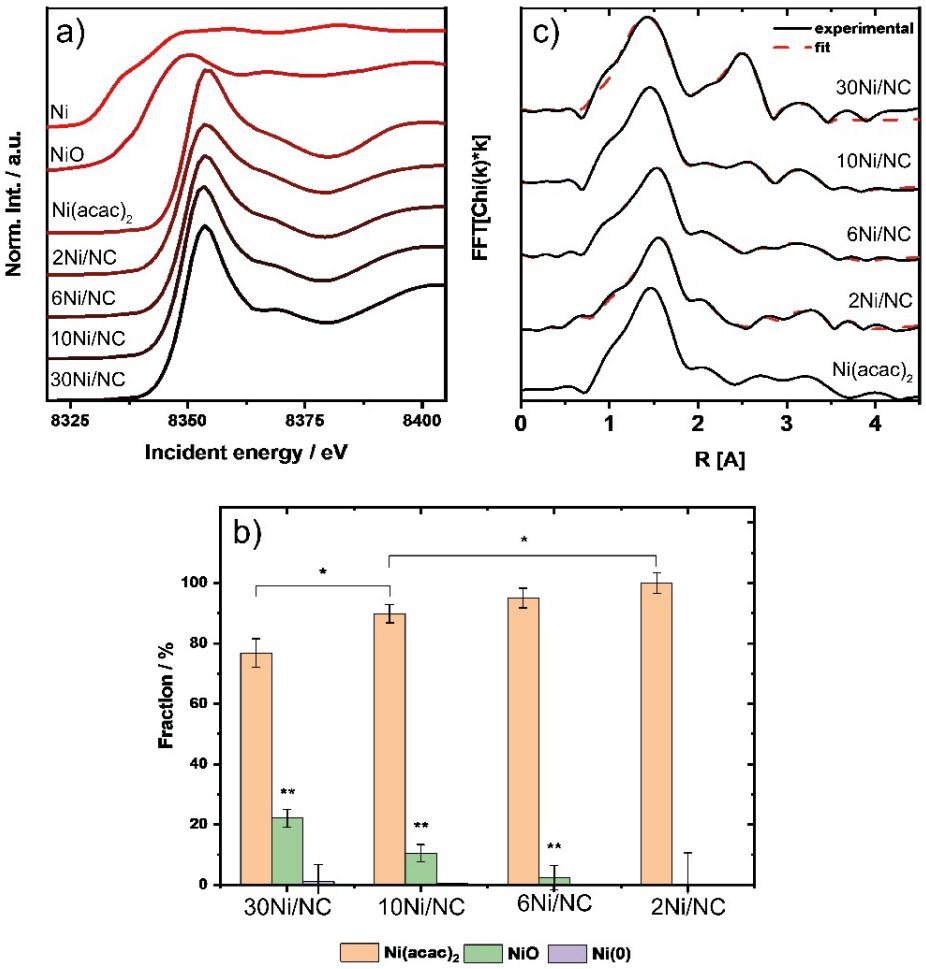

Figure 3. (a) Normalized XANES spectra of Ni, NiO, $Ni(acac)_2$, and $_X$Ni/NC samples. (b) Linear combination fitting of $_X$Ni/NC samples with references Ni(0), NiO, and $Ni(acac)_2$. * and ** marks statistically significant differences at $p < 0.05$ for $Ni(acac)_2$ and NiO respectively. (c) Fourier-transformed EXAFS spectra of $_X$Ni/NC samples along with fitted models (no phase correction applied).

Ni K-edge EXAFS was collected to assess the local coordination environment of the Ni atoms in nickel decorated samples in comparison to the Ni, NiO, and $Ni(acac)_2$ references. The k-weighted Fourier transform of the EXAFS of 2Ni/NC, 6Ni/NC, and 10Ni/NC with corresponding fits and reference samples are shown in **Figure 3c**. The EXAFS analysis was conducted based on the theoretical structure (vide infra). The values of the coordination numbers and atomic distances are the averages of all Ni centers within the probed sample, leading to relatively large Debye-Waller factors. The exact values of the EXAFS fit are presented in **Table S3-6**. This analysis depicts a prominent first shell Ni-O scatter at ca. 2.035 Å. The average coordination number is reduced from 6 for 2Ni/NC to 3 for 30Ni/NC. The

atomic distances are in agreement with the oxygen coordination environment reported in the literature for nickel oxide.[45] Only multiple scattering Ni-C-Ni paths were detected in the EXAFS signal of 2Ni/NC and 6Ni/NC, which is consistent with the presence of dispersed, isolated Ni centres in these samples. In particular, Ni-Ni pair at 2.6 Å reflecting metallic Ni could be fitted, which demonstrates that in agreement with the LC-XANES fit, only a minor fraction of Ni metal (nano)clusters are present in 2Ni/NC and 6Ni/NC.[46] However, an increasing second coordination shell peak at 3.044 Å in 10Ni/NC and 3.0 Å 30Ni/NC is similar to the Ni-Ni distance of bulk NiO (2.94 Å) and indicates oxide clusters in these samples, which is in good agreement with the information obtained from XPS data. The information extracted from STEM analyses, XPS, Ni K-edge XANES, and EXAFS demonstrates the presence of dispersed Ni atoms in 2Ni/NC and 6Ni/NC coordinated by oxygen and the presence of larger clusters and nanoparticles of oxidized nickel in 10Ni/NC and 30Ni/NC, respectively. The nearest neighbour shells at around 1.5 Å suffers from the limitation of EXAFS to distinguish light atom backscatters, such as carbon and oxygen. The obtained coordination numbers and assignments given in **Table S3-S6** should thus be understood as estimation, in particular as all species and their light atom coordination are averaged.

The performed DFT-based dynamical simulated annealing (composition and cell parameter in **Table S7**) leads to optimized structures of 6Ni/NC and 10Ni/NC, which are shown in **Figure 4**. In accordance with XPS and EXAFS findings, calculations were made considering nickel atoms in oxidation state +II. Coordination numbers obtained from the radial distribution functions of the simulated materials (**Figure S5**) indicate that the nickel coordination environment at distances under 2.4 Å is mainly composed by oxygen for both samples with two oxygen atoms in the vicinity, one carbon and one nitrogen each (see **Table 2**). This goes along with the XPS and EXAF findings. The oxygen atoms are carrying a partial negative charge in 6Ni/NC (-0.28) and 10Ni/NC (-0.26), which stabilize the nickel atoms (see **Table S8**). The presence of equal amounts of nitrogen (-0.21 and -0.18) and carbon atoms (+0.20 and +0.21) in

the coordination environment of nickel atoms, while having an overall C/N ratio of 3:1, indicate that nitrogen helps stabilizing the system. Herein, is worth keeping in mind that the absence of a clear increase of the contribution of the N-metal band in the N1s XPS spectra indicates the role of nitrogen atoms in the stabilization of nickel but not forming direct coordination bonds to the nickel atoms but probably by only helping dispersing the original organic salt and preventing clustering during heat treatment. The distribution of the negative charge in the electrocatalysts can also be seen at the electron density isosurfaces on the r. h. s. of **Figure 4**, where the electrons density is significantly higher at the oxygen and nitrogen atoms as compared to the partial positive carbons. Systems with similar C/N ratio as 6Ni/NC and 10Ni/NC, but no oxygen (herein, 6Ni/NC-Ofree and 10Ni/NC-Ofree), were investigated to understand the contribution of the support to the stabilization of nickel (**Figure S6-S7** and **Table 2**). The larger Ni-N coordination number of 6Ni/NC-Ofree over that of 10Ni/NC-Ofree indicates that at lower loading the contribution of nitrogen to the stabilization of nickel gain more importance than at larger loadings. These findings also go along with the results obtained by EXAF and XPS, which indicate in sample 10Ni/NC the presence of already significant amounts of NiO clusters, whereas in sample 6Ni/NC Ni exists mainly in the form of single sites.

Table 2. Nickel coordination numbers obtained by integrating radial distribution functions ($d_{Ni-X} < 2.4$ Å) of simulated 6Ni/NC and 10Ni/NC and their oxygen free analogues.

	Overall	**C**	**N**	**O**	**Ni**
6Ni/NC-Ofree	4.65	2.48	2.09	-	0.08
6Ni/NC	4.56	1.17	1.19	2.15	0.04
10Ni/NC-Ofree	4.46	2.41	1.89	-	0.15
10Ni/NC	4.99	1.18	1.45	2.29	0.07

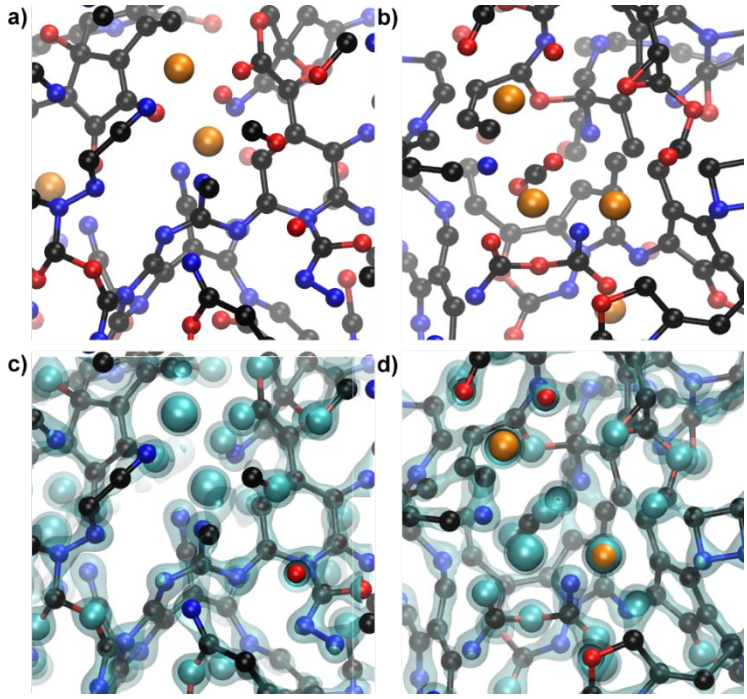

Figure 4. Snapshot of the modeled lowest energy structures of samples (a) 6Ni/NC and (b) 10Ni/NC. Colour code: carbon (black), nitrogen (blue), oxygen (red), nickel (orange). Electron density isosurfaces of the same area of (c) 6Ni/NC and (d) 10Ni/NC structures. The highest electron density (disregarding Ni) is located around oxygen atoms (solid cyan isosurface; isovalue = 0.6). The density is lower around nitrogen atoms (transparent surface; isovalue = 0.25). The lowest values are found around the carbon atoms.

Prior to electrochemical analyses, also the textural properties of the samples were analysed by N_2 and CO_2 adsorption/desorption isotherms at 77 K and 273 K, respectively. Samples NC, 2Ni/NC, 6Ni/NC, and 10Ni/NC show a type I N_2 sorption isotherm, indicating that their porous network is mainly formed by micro- and macropores (**Figure S8a**). Samples 2Ni/NC and 6Ni/NC exhibit surface areas of ca. 1800 m^2/g and a total pore volume of ca. 1 cm^3/g (see **Table 1**) (i.e., pretty similar to NC, further indicating that the support survived the thermal treatment despite the oxidative atmosphere and the nickel content of the mixes).[29] However, at higher nickel loadings, the porosity of the samples starts collapsing. For instance, the total pore volume of 10Ni/NC is ca. 0.55 cm^3/g, i.e., half than that of NC, 2Ni/NC, and 6Ni/NC (**Table 1**). Interestingly, CO_2 sorption isotherms at 273 K in **Figure S8b** show how all 2Ni/NC, 6Ni/NC, and 10Ni/NC show a very similar CO_2 sorption capacity of ca. 5 mmol/g (and micropore volume of ca. 0.20 cm^3/g, Table 1) as the support.[29] Though 10Ni/NC exhibits half of the

total pore volume of the original substrate, its composition is near $C_3NO_{0.5}Ni_{0.15}$. CN frameworks are known to adsorb CO_2 in structural pores.[31, 47, 48] Despite the dramatic decrease in total pore volume, the change in composition explains the high sorption capability of 10Ni/NC. When the nickel loading further increases (i.e., sample 30Ni/NC), the much larger nickel content makes the composition change to $C_4NO_{1.5}Ni_{0.8}$. The much lower pore volume obtained from both N_2 and CO_2 isotherms (0.11 and 0.03 cm^3/g) and the larger carbon content indicate the collapse of the porous network that is also Ni saturated with almost one nickel atom per C_4N unit.

Electrochemical CO_2 reduction

The electrochemical performance of $_X$Ni/NC samples was first evaluated by linear sweep voltammetry (LSV). **Figure 5a** shows very different behavior in $_X$Ni/NC samples upon Ni loading, indicating that the Ni single atoms and clusters are modifying the electrochemical properties of NC. On the other hand, LSVs of 10Ni/NC in Ar and CO_2-saturated NaOH solution show that this sample exhibited a lower onset potential (-1.163 V vs RHE) and current density (1.07 A/g at -1.303 V vs RHE) in the CO_2 saturated solution indicating a remarkable activity in the CO_2RR (**Figure 5b**). Additionally, LSVs of NC in Ar and CO_2-saturated NaOH solutions showed no activity for CO_2RR, indicating that Ni single atoms or sub-nanometric clusters are the active sites for this reaction (**Figure S9**).

The electrochemical activity of $_X$Ni/NC samples in CO_2-saturated NaOH solutions was evaluated as a function of Ni loading. It is worth mentioning that 2Ni/NC behaved identically to NC, and therefore, its electrochemical activity will not be included in this study.[49, 50] LSVs of 6Ni/NC, 10Ni/NC, and 30Ni/NC are presented in **Figure 5c**. 10Ni/NC featured a higher current density than 6Ni/NC, probably due to its higher Ni content (11 wt% vs. 6 wt%). However, despite the overall Ni loading being higher for 30Ni/NC (33 wt%), the sample

exhibited the lowest current density, probably due to the negative effect that the formation of NiO nanoparticles has on the decrease of low-coordinated surface atoms ratio.

The products obtained in the gas and liquid phases were analyzed by on-line GC and off-line HPLC, respectively. H_2, CO, and CH_4 were detected as gas products by GC. Surprisingly, HCOOH was detected in the liquid phase by HPLC and verified by ^1H nuclear magnetic resonance (NMR) (see **Figure S10** in Supplementary Information). It must be highlighted that there are no precedents in the literature of HCOOH evolution from carbon-based electrodes containing Ni single atoms or clusters. For instance, such materials typically exhibit nearly 100% Faradaic efficiency (FE) towards CO.[51-54] As mentioned in the introduction, it has been reported that nickel coordinated to oxygen over carbonaceous supports can exhibit very different electrochemical selectivity than nitrogen coordinated nickel when used as electrocatalysts for both ORR[26, 27] and CO_2RR.[28] Herein, single nickel atoms and/or clusters coordinated to oxygen foster the unexpected production of HCOOH.

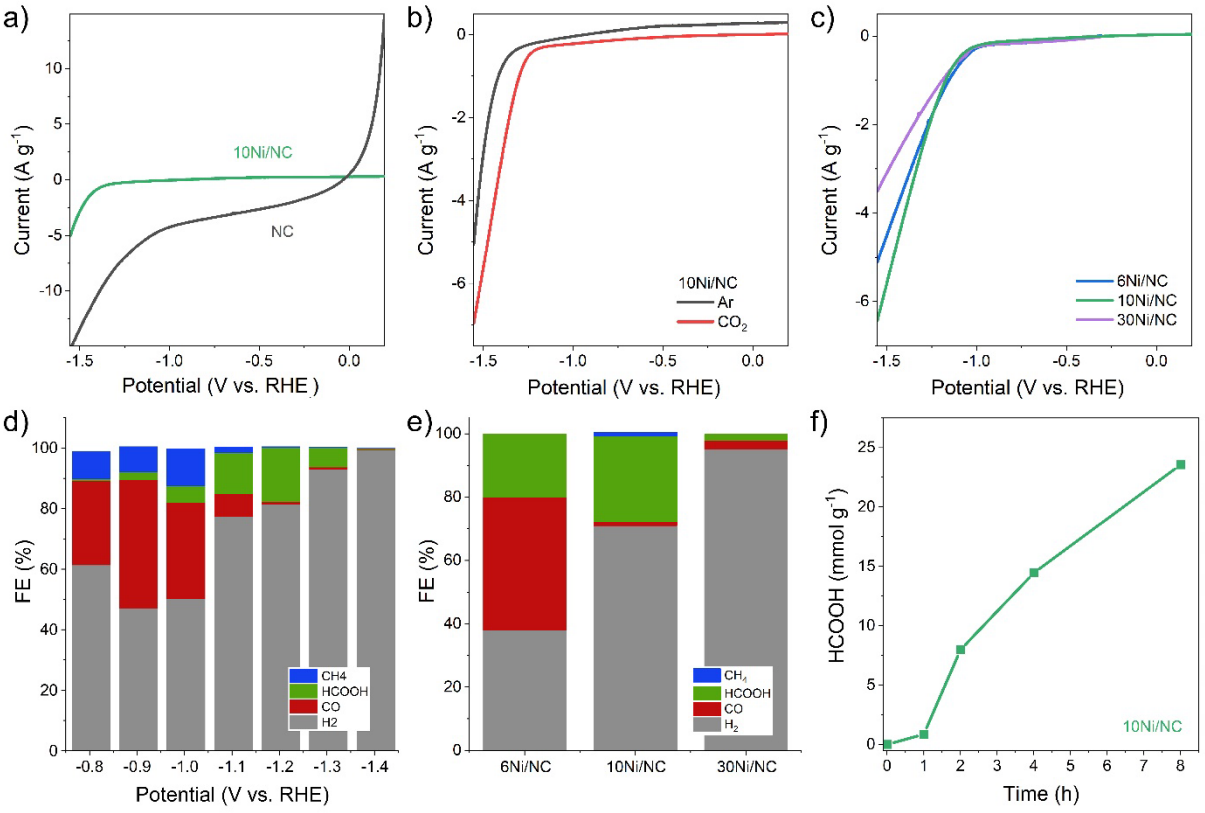

Figure 5. (Top) LSVs of NC and 10Ni/NC in Ar-saturated 1M NaOH solution (a), 10Ni/NC first in Ar- and then CO_2-saturated 1M NaOH solution (b), and 6Ni/NC, 10Ni/NC, and 30Ni/NC

in CO_2-saturated 1M NaOH solution (c). LSVs were carried out at 50 mV/s. (Bottom) CH_4 (yellow), HCOOH (blue), CO (red), and H_2 (black) FE vs. applied potential of 10Ni/NC samples in CO_2-saturated 1M NaOH solution (d), FE of 6Ni/NC, 10Ni/NC, and 30Ni/NC at -1.2 V vs RHE in CO_2-saturated 1M NaOH solution for 4 h (e) and HCOOH concentration evolution as using 10Ni/NC as a catalyst for the CO_2RR (f).

Figure 5d shows the FEs towards different products obtained for the sample 10Ni/NC at different potentials after 4h. FEs of the different gas products were obtained by inline gas chromatography, whereas liquid products were analysed by HPLC. As can be seen, the gas phase is mainly composed of CO and CH_4 at potentials below -1.0 V vs RHE, while HCOOH becomes the CO_2RR main product at potential ranging from -1.1 to -1.3 V vs RHE. At larger potentials, H_2 is practically the only detectable reaction product. Control experiments in Ar-saturated 1M NaOH solutions were also carried out obtaining undetectable amounts of CO, CH_4, or HCOOH. The 10Ni/NC Tafel slope was 238 mV/dec (**Figure S11** in Supplementary Information). This huge value indicates that there are mass transfer limitations, probably due to large volumes of micropores and no mesopores. Thus, the slope holds no information about CO_2RR kinetics.[55] Further studies to understand the mechanism behind CO_2RR over subnanometric oxygen coordinated-Ni clusters supported on doped, noble-carbonaceous materials are undergoing.

Chronoamperometry (CA) in CO_2-saturated NaOH solution at -1.2 V vs RHE was carried out with the different samples for 8h (see **Figure S12** in Supplementary Information). The results show that, despite the oxidation state of nickel on the samples, the electrodes are stable in the experimental conditions. This surprising behaviour has already been reported several times and was recently reviewed by Yeo et al.[56] For instance, according to the nickel electrochemical phase diagram, Ni^{+2} is stable up to -1V.[57] Here, we must hypothesize that the oxidative noble carbonaceous support on which nickel is loaded plays a key role in stabilizing nickel as single sites. Indeed, the stabilization of electron-poor transition metals to oxygen sites in graphene-like carbons is possible.[46] FEs towards the different products obtained using 6Ni/NC, 10Ni/NC, and 30Ni/NC after four-hour CO_2RR experiments at -1.2 V vs RHE are compared in

Figure 5e. As can be observed, 6Ni/NC features FEs for CO, H_2, and HCOOH of ~ 42%, 37%, and 20%, respectively. Sample 10Ni/NC presents FEs for H_2 and HCOOH of ~ 71% and 27%, respectively. However, the FEs for CO and CH_4 were ~ 1%. Finally, 30Ni/NC showed a FE for H_2 of ca. 95%, being those of CO and HCOOH of approximately 2%. Long-term experiments at 8h showed that neither CO and H_2 concentration decrease nor the formation of any other product, with FE of all products being nearly constant along the reaction time. In this regard, **Figure 5f** shows how HCOOH production follows a linear trend with time, indicating that the catalysts do not deactivate with time, which further proves the stability of the samples.

Given these results, one can anticipate that both the way Ni is loaded and its interaction with the support have a strong influence on CO_2RR selectivity. In contrast with existing literature, where CO has been found as the only product of CO_2RR, the formation of Ni sites with high oxidation state and stabilized in oxygen coordination environment instead of nitrogen in 6Ni/NC favours CO and HCOOH to be the main CO_2RR products observed. When the Ni loading increase in 10Ni/NC, a sharp decrease in the CO evolution is observed (FE towards CO changes from 42% to 1% for samples 6Ni/NC and 10Ni/NC, respectively), and HCOOH production raises from 7.8 to 14.5 mmol/g with an unprecedented FE that goes from 20% to 27% at 1.3 to 1.5 V, respectively. It is reasonable to hypothesize that a mixture of Ni(II) and Ni(III) could be present in 6Ni/NC and 10Ni/NC (**Figure 2c** and **Figure 2d**), although in different extents due to the different population of single sites and Ni-O subnanometric clusters that they present. These differences foster the production of HCOOH rather than CO. In view of the present results, we can speculate that increasing Ni loading would induce changes in the Ni oxidation state up to an optimum value that would inhibit the CO evolution and leave HCOOH as the main CO_2RR product in 10Ni/NC. Further increase in the Ni loading results in the collapse of the carbonaceous network stabilizing Ni sites and consequently in the formation of 5 nm NiO nanoparticles, which all in all inhibits the CO_2RR and favors HER. Thus, careful

design of the catalyst considering support composition, interaction with the metal and optimum size of the catalytic are responsible for the remarkable changes in the CO_2RR product selectivity.

3. Conclusion

Subnanometric nickel active sites for the CO_2 reduction reaction were loaded over a noble carbonaceous material derived from cytosine using a simple multigram like process consisting only of two steps: (1) the impregnation of the support with nickel (II) acetylacetonate plus (2) subsequent calcination at 350°C in air. Up to 11 wt% of Ni subnanometric sites were loaded using this approach. High Ni loadings promote the stabilization of CxNO frameworks rather than simple graphitization of the support. The highly oxidative nature of the support and the use of a Ni-O4 coordinated precursor salt foster a high oxidation state of nickel, as EXAFS analyses corroborate. The highly N-doped carbonaceous network helps stabilizing large Ni-clusters and nanoparticles. Unlike N-coordinated nickel subnanometric sites, the oxygen coordinated ones show unprecedented FE of 20 - 27 % towards HCOOH at 1.3 - 1.5 V vs. RHE. At higher loadings (33 wt% of Ni), NiO nanoparticles form, and HER predominates. The strong dependence of the Ni loading and support interactions with the electrocatalytic activity in the CO_2RR open new design paths for the preparation of transition metal single-site catalysts.

4. Experimental Section/Methods

Materials and synthetic description

Materials: Cytosine (99%) and zinc chloride were purchased from Merck. Sodium chloride (98%) and Nafion solution (5wt%) were purchased from Sigma Aldrich. 95% nickel (II) bis(acetylacetonate) (herein, $Ni(acac)_2$) was purchased from Alfa Aesar. Hydrochloric acid (37%), sulfuric acid (96%), and sodium hydroxide (>98%) were purchased from Roth. Synthesis grade acetone was purchased from J.T. Baker. All chemicals were used as received without further purification.

Support synthesis: The carbonaceous support was prepared as described in ref. . In brief, Cytosine (1 g) was grinded with 20 g of a mixture 1:1 wt% of NaCl and $ZnCl_2$ at room temperature. The mixture was treated thermally at 800°C (2h, 1°C/min) in a nitrogen atmosphere. The obtained solid was allowed to cool down and washed 3 times in HCl 1M at room temperature to remove the NaCl and $ZnCl_2$ salts from the carbonaceous material. After the washing steps, 300mg of a bulky black powder was obtained. The sample will be labelled "NC" henceforth.

Ni deposition: NC (100 mg) was mixed with different amounts of $Ni(acac)_2$ (10 mg, 30 mg, 50 mg, 70 mg) and acetone (5 mL). The system was stirred at room temperature for 1h. Acetone was completely evaporated at 70°C. The residual solid was transferred to a crucible, and it was submitted to thermal treatment at 350°C (2h, 1°C/min) in air. The obtained samples were labelled according to the final loading of nickel found in the samples as 2Ni/NC, 6Ni/NC, 10Ni/NC, and 30Ni/NC which corresponded to 10 mg, 30 mg, 50 mg, and 70 mg of $Ni(acac)_2$ used in the synthesis, respectively.

Characterization procedures

Powder X-ray diffraction (XRD) patterns were recorded using a Bruker D8 Advance instrument with Cu-Kα radiation. Thermogravimetric analyses (TGA) were performed from 25 to 1000°C in a NETZSCHTG 209 F1 device, using either nitrogen or synthetic air as a carrier gas and a heating rate of 10K/min in a Pt crucible. Inductively coupled plasma optical emission spectrometry (ICP-OES) measurements were performed with a PerkinElmer ICP-OES Optima 8000. Before measurement, the samples (0.01 g) were dissolved in 500 µl of a 1:3 mixture of concentrated HCl and HNO_3 acids for 12 hours at room temperature and finally heated for 1 hour at 96°C. The obtained solution was diluted up to 10 ml with ultrapure Milli-Q water and filtrated before ICP-OES measurements. The morphology of the samples was characterized by scanning electron microscopy (SEM), using a LEO 1550-Gemini instrument from Zeiss. For this, the samples were sputter-coated with a few nanometres of an 80% Au/20% Pd alloy to

reach sufficient surface conductivity. With this instrument, energy-dispersive X-ray spectroscopy (EDX) was conducted as well, using a coupled Oxford Instruments EDX analyser. Transmission electron microscopy (TEM) and scanning transmission electron microscopy (STEM) were carried out utilizing a Zeiss EM 912, equipped with a LaB_6 cathode and operated at 120 keV, and a double-Cs-corrected JEOL ARM200F, equipped with a field emission gun and operated at 80 keV. The dimension and the density of the single site spot are obtained from dark field images using Fiji software and counting 100 points. Nitrogen adsorption and desorption isotherms at 77 K and CO_2 adsorption and desorption isotherms at 273 K (ice-water bath) were measured using a Quantachrome Quadrasorb SI apparatus. The samples were degassed at 150°C under vacuum for 20h prior to each measurement. The specific surface area of each material was obtained from the nitrogen adsorption data ($P/P_0 < 0.2$) using the Brunauer-Emmett-Teller (BET) method. The value was obtained after applying the method in the linear region with the best correlation. Total pore volume (V_T) was calculated from the amount of nitrogen adsorbed at $P/P_0=0.995$. The N_2 pore size distribution was obtained by Quenched Solid Density Functional Theory (QSDFT) model with slit/cylindrical pore shape using nitrogen adsorption data at 77K. Microporous volume (V_{mic}) was calculated applying the DFT method to the adsorption branch of CO_2 isotherms. X-ray photoemission spectroscopy (XPS) was measured on a SPECS spectrometer equipped with a Phoibos 150 9MCD detector using a nonmonochromatic X-ray source (Al and Mg) operating at 200 W. The samples were evacuated in the pre-chamber of the spectrometer at 1×10^{-9} mbar. The measured ratios of the components were obtained from the area of the corresponding peaks after nonlinear Shirley-type background subtraction and corrected by the transition function of the spectrometer. The Ni K edge X-ray absorption fine structure (XAFS) was recorded in transmission mode at mySpot beamline at Bessy II.[58, 59] The energy calibration was done at first inflection point of Ni(0) XANES spectrum (8333 eV). Energy selection was performed with Si(111) multiple crystal monochromator, and signal detection was conducted using ionization chamber with air. The

beam spot size on sample was 0.5 mm and total flux of $1.5x10^{11}$ ph/s.[58] The analysis of extended x-ray absorption fine structure (EXAFS) was performed using Athena and Artemis software.[60]

Electrocatalytic tests: xNi/NC samples (10 mg) were dispersed in ethanol solution (200 μL) containing 50 μL of Nafion 117 solution (~ 5%) from Sigma-Aldrich, and sonicated until a homogeneous ink was obtained. The working electrodes were prepared, drop-casting 30 μL of the as-prepared ink on each side of a gas diffusion layer of carbon paper (1.5 cm x 1 cm) (Spectracarb 2050-0550 from FuelCellStore) and allowed for solvent evaporation at room temperature. Then, the xNi/NC electrodes were vacuum dried overnight to remove all solvent traces. The electrochemical characterization was carried out with an electrochemical workstation (Gamry Interface 1000). CO_2RR was evaluated in a custom-made three-electrode H-cell configuration, separated by Nafion 117 membrane (Scheme S1). The reference and counter electrodes used were Ag/AgCl KCl saturated and Pt foil, respectively. 1M NaOH aqueous solution was used as the electrolyte. Catalytic performance tests were carried out using chronoamperometry measurements at different potentials. Gas products were detected by gas chromatography (GC) using a Shimadzu GC-2014. H_2 was quantified with a MolSieve 5A column by TC detector, while CO and CH_4 were analyzed with a PorePlot Q column by FI detector. High-performance liquid chromatography (HPLC) was performed to analyze the liquid phase produces using a Dionex UltiMate 3000 UHPLC system, which consisted of an UltiMate 3000 RS pump, an UltiMate 3000 RS autosampler, an UltiMate 3000 RS column compartment, and UltiMate 3000 RS Variable wavelength detector (Dionex Sortfon GmbH, Germany). A Rezex™ ROA-Organic Acid H^+ LC Column (300 x 7.8 mm) from Phenomenex was used. The samples were acidified with H_2SO_4 up to pH 2-3. The measurements were carried out with an H_2SO_4 solution (0.005 N) as a mobile phase at 0.5 mL/min flow rate at 25°C.

Computational details

Periodic density functional theory (DFT) calculations were carried out using the hybrid Gaussian and plane wave approach,[61] as implemented in the CP2K/Quickstep code.[62] The Kohn-Sham orbitals were described by an accurate molecularly optimized double-zeta basis set with one additional set of polarization function,[63] while the charge density was represented by plane waves with a density cut-off of 500 Ry. The B97-3c exchange and correlation functional plus a damped atom-pairwise dispersion correction to account for long-range van der Waals interactions was employed.[64] Separable norm-conserving pseudopotentials were used to mimic the interactions between the valence electrons and the ionic cores.[65] The electrocatalysts 6Ni/NC and 10Ni/NC, as well as oxygen-free reference structures were modelled according to the experimentally compositions. The systems are charged to represent Ni atoms in oxidation state +II. The exact composition of the theoretical models and their associated supercell parameters can be found in **Table S1**. Optimized structures of the electrocatalysts were obtained by globally minimizing the potential energy, while varying the atomic positions by dynamical simulated annealing based on the second-generation Car-Parrinello approach of Kühne et al.[66-68] The net atomic charges (NACs) of these structures are calculated using the density derived electrostatic and chemical method DDEC6.[69] In order to calculate the radial distribution functions at finite temperature, the optimized structures were additionally simulated for 160 ps using a discretized time step of 2.0 fs by means of extended tight binding (xTB)[70] molecular dynamics in the canonical ensemble at 300 K.

Acknowledgements

Max Planck Society is greatly acknowledge for its financial support. Heike Runge and Rona Pitschke are acknowledged for their contribution analyzing the samples through SEM.

References

[1] B. Khezri, A.C. Fisher, M. Pumera, CO2 reduction: the quest for electrocatalytic materials, Journal of Materials Chemistry A 5(18) (2017) 8230-8246.
[2] L. Dai, Q. Qin, P. Wang, X. Zhao, C. Hu, P. Liu, R. Qin, M. Chen, D. Ou, C. Xu, S. Mo, B. Wu, G. Fu, P. Zhang, N. Zheng, Ultrastable atomic copper nanosheets for selective electrochemical reduction of carbon dioxide, Science Advances 3(9) (2017) e1701069.
[3] J. Wu, S. Ma, J. Sun, J.I. Gold, C. Tiwary, B. Kim, L. Zhu, N. Chopra, I.N. Odeh, R. Vajtai, A.Z. Yu, R. Luo, J. Lou, G. Ding, P.J.A. Kenis, P.M. Ajayan, A metal-free electrocatalyst for carbon dioxide reduction to multi-carbon hydrocarbons and oxygenates, Nature Communications 7(1) (2016) 13869.
[4] L. Fan, C. Xia, F. Yang, J. Wang, H. Wang, Y. Lu, Strategies in catalysts and electrolyzer design for electrochemical CO₂ reduction toward C₂₊ products, Science Advances 6(8) (2020) eaay3111.
[5] M. Lefèvre, E. Proietti, F. Jaouen, J.-P. Dodelet, Iron-Based Catalysts with Improved Oxygen Reduction Activity in Polymer Electrolyte Fuel Cells, Science 324(5923) (2009) 71-74.
[6] D. Malko, A. Kucernak, T. Lopes, In situ electrochemical quantification of active sites in Fe–N/C non-precious metal catalysts, Nature Communications 7(1) (2016) 13285.
[7] S. Kuld, M. Thorhauge, H. Falsig, C.F. Elkjær, S. Helveg, I. Chorkendorff, J. Sehested, Quantifying the promotion of Cu catalysts by ZnO for methanol synthesis, Science 352(6288) (2016) 969-974.
[8] G. Chen, C. Xu, X. Huang, J. Ye, L. Gu, G. Li, Z. Tang, B. Wu, H. Yang, Z. Zhao, Z. Zhou, G. Fu, N. Zheng, Interfacial electronic effects control the reaction selectivity of platinum catalysts, Nature Materials 15(5) (2016) 564-569.
[9] W. Bi, X. Li, L. Zhang, T. Jin, L. Zhang, Q. Zhang, Y. Luo, C. Wu, Y. Xie, Molecular co-catalyst accelerating hole transfer for enhanced photocatalytic H2 evolution, Nature Communications 6(1) (2015) 8647.
[10] L. Liu, A. Corma, Metal Catalysts for Heterogeneous Catalysis: From Single Atoms to Nanoclusters and Nanoparticles, Chem. Rev. 118(10) (2018) 4981-5079.
[11] S. Mitchell, E. Vorobyeva, J. Pérez-Ramírez, The Multifaceted Reactivity of Single-Atom Heterogeneous Catalysts, Angewandte Chemie International Edition 57(47) (2018) 15316-15329.
[12] Z. Li, S. Ji, Y. Liu, X. Cao, S. Tian, Y. Chen, Z. Niu, Y. Li, Well-Defined Materials for Heterogeneous Catalysis: From Nanoparticles to Isolated Single-Atom Sites, Chemical Reviews 120(2) (2020) 623-682.
[13] R. Reske, H. Mistry, F. Behafarid, B. Roldan Cuenya, P. Strasser, Particle Size Effects in the Catalytic Electroreduction of CO2 on Cu Nanoparticles, Journal of the American Chemical Society 136(19) (2014) 6978-6986.
[14] T.N. Huan, N. Ranjbar, G. Rousse, M. Sougrati, A. Zitolo, V. Mougel, F. Jaouen, M. Fontecave, Electrochemical Reduction of CO2 Catalyzed by Fe-N-C Materials: A Structure–Selectivity Study, ACS Catalysis 7(3) (2017) 1520-1525.

[15] T.W. van Deelen, C. Hernández Mejía, K.P. de Jong, Control of metal-support interactions in heterogeneous catalysts to enhance activity and selectivity, Nature Catalysis 2(11) (2019) 955-970.
[16] L. He, F. Weniger, H. Neumann, M. Beller, Synthesis, Characterization, and Application of Metal Nanoparticles Supported on Nitrogen-Doped Carbon: Catalysis beyond Electrochemistry, Angewandte Chemie International Edition 55(41) (2016) 12582-12594.
[17] M. Antonietti, M. Oschatz, The Concept of "Noble, Heteroatom-Doped Carbons," Their Directed Synthesis by Electronic Band Control of Carbonization, and Applications in Catalysis and Energy Materials, Adv. Mater. 30(21) (2018).
[18] S. Zhang, K. Dokko, M. Watanabe, Carbon materialization of ionic liquids: from solvents to materials, Materials Horizons 2(2) (2015) 168-197.
[19] D.W. Ma, Q. Wang, X. Yan, X. Zhang, C. He, D. Zhou, Y. Tang, Z. Lu, Z. Yang, 3d transition metal embedded C<inf>2</inf>N monolayers as promising single-atom catalysts: A first-principles study, Carbon 105 (2016) 463-473.
[20] W. Zhong, Y. Liu, M. Deng, Y. Zhang, C. Jia, O.V. Prezhdo, J. Yuan, J. Jiang, C<inf>2</inf>N-supported single metal ion catalysts for HCOOH dehydrogenation, Journal of Materials Chemistry A 6(24) (2018) 11105-11112.
[21] X. Cui, W. An, X. Liu, H. Wang, Y. Men, J. Wang, C<inf>2</inf>N-graphene supported single-atom catalysts for CO<inf>2</inf> electrochemical reduction reaction: mechanistic insight and catalyst screening, Nanoscale 10(32) (2018) 15262-15272.
[22] X. Zhang, A. Chen, Z. Zhang, M. Jiao, Z. Zhou, Transition metal anchored C<inf>2</inf>N monolayers as efficient bifunctional electrocatalysts for hydrogen and oxygen evolution reactions, Journal of Materials Chemistry A 6(24) (2018) 11446-11452.
[23] F. Pan, W. Deng, C. Justiniano, Y. Li, Identification of champion transition metals centers in metal and nitrogen-codoped carbon catalysts for CO<inf>2</inf> reduction, Applied Catalysis B: Environmental 226 (2018) 463-472.
[24] Z. Cai, P. Du, W. Liang, H. Zhang, P. Wu, C. Cai, Z. Yan, Single-atom-sized Ni–N4 sites anchored in three-dimensional hierarchical carbon nanostructures for the oxygen reduction reaction, Journal of Materials Chemistry A 8(30) (2020) 15012-15022.
[25] Z. Zhu, H. Yin, Y. Wang, C.H. Chuang, L. Xing, M. Dong, Y.R. Lu, G. Casillas-Garcia, Y. Zheng, S. Chen, Y. Dou, P. Liu, Q. Cheng, H. Zhao, Coexisting Single-Atomic Fe and Ni Sites on Hierarchically Ordered Porous Carbon as a Highly Efficient ORR Electrocatalyst, Adv Mater 32(42) (2020) e2004670.
[26] X. Song, N. Li, H. Zhang, L. Wang, Y. Yan, H. Wang, L. Wang, Z. Bian, Graphene-Supported Single Nickel Atom Catalyst for Highly Selective and Efficient Hydrogen Peroxide Production, ACS Applied Materials & Interfaces 12(15) (2020) 17519-17527.
[27] Y. Wang, R. Shi, L. Shang, G.I.N. Waterhouse, J. Zhao, Q. Zhang, L. Gu, T. Zhang, High-Efficiency Oxygen Reduction to Hydrogen Peroxide Catalyzed by Nickel Single-Atom Catalysts with Tetradentate N2O2 Coordination in a Three-Phase Flow Cell, Angew. Chem. Int. Ed. 59(31) (2020) 13057-13062.
[28] J.E. Pander III, D. Ren, Y. Huang, N.W.X. Loo, S.H.L. Hong, B.S. Yeo, Understanding the Heterogeneous Electrocatalytic Reduction of Carbon Dioxide on Oxide-Derived Catalysts, ChemElectroChem 5(2) (2018) 219-237.
[29] A. Rodríguez-Gómez, E. Lepre, L. Sánchez-Silva, N. López-Salas, A.R. de la Osa, PtRu nanoparticles supported on noble carbons for ethanol electrooxidation, Journal of Energy Chemistry 66 (2022) 168-180.
[30] P. Kuhn, A. Forget, D. Su, A. Thomas, M. Antonietti, From Microporous Regular Frameworks to Mesoporous Materials with Ultrahigh Surface Area: Dynamic Reorganization of Porous Polymer Networks, Journal of the American Chemical Society 130(40) (2008) 13333-13337.

[31] J. Kossmann, T. Heil, M. Antonietti, N. López-Salas, Guanine-Derived Porous Carbonaceous Materials: Towards C1N1, ChemSusChem 13(24) (2020) 6643-6650.
[32] F.J. Maldonado-Hódar, C. Moreno-Castilla, J. Rivera-Utrilla, Y. Hanzawa, Y. Yamada, Catalytic Graphitization of Carbon Aerogels by Transition Metals, Langmuir 16(9) (2000) 4367-4373.
[33] J. Tang, T. Wang, X. Sun, Y. Guo, H. Xue, H. Guo, M. Liu, X. Zhang, J. He, Effect of transition metal on catalytic graphitization of ordered mesoporous carbon and Pt/metal oxide synergistic electrocatalytic performance, Microporous and Mesoporous Materials 177 (2013) 105-112.
[34] A. Furlan, J. Lu, L. Hultman, U. Jansson, M. Magnuson, Crystallization characteristics and chemical bonding properties of nickel carbide thin film nanocomposites, J Phys Condens Matter 26(41) (2014) 415501.
[35] A.V. Vorontsov, S.V. Tsybulya, Influence of Nanoparticles Size on XRD Patterns for Small Monodisperse Nanoparticles of Cu0 and TiO2 Anatase, Industrial & Engineering Chemistry Research 57(7) (2018) 2526-2536.
[36] M. Barber, J.A. Connor, M.F. Guest, M.B. Hall, I.H. Hillier, W.N.E. Meredith, High energy photoelectron spectroscopy of transition metal complexes. Part 1.—Bonding in substituted and unsubstituted first row carbonyls, Faraday Discussions of the Chemical Society 54(0) (1972) 219-226.
[37] T. Weiss, J. Warneke, V. Zielasek, P. Swiderek, M. Bäumer, XPS study of thermal and electron-induced decomposition of Ni and Co acetylacetonate thin films for metal deposition, Journal of Vacuum Science & Technology A 34(4) (2016) 041515.
[38] L. Xie, X. Ren, Q. Liu, G. Cui, R. Ge, A.M. Asiri, X. Sun, Q. Zhang, L. Chen, A Ni(OH)2–PtO2 hybrid nanosheet array with ultralow Pt loading toward efficient and durable alkaline hydrogen evolution, Journal of Materials Chemistry A 6(5) (2018) 1967-1970.
[39] R.H. Aguilera-del-Toro, F. Aguilera-Granja, L.C. Balbás, A. Vega, Structure, fragmentation patterns, and magnetic properties of small nickel oxide clusters, Physical Chemistry Chemical Physics 19(4) (2017) 3366-3383.
[40] M. Bauer, H. Bertagnolli, X-Ray Absorption Spectroscopy – the Method and Its Applications, Methods in Physical Chemistry, pp. 231-269.
[41] N. Prinz, L. Schwensow, S. Wendholt, A. Jentys, M. Bauer, W. Kleist, M. Zobel, Hard X-ray-based techniques for structural investigations of CO2 methanation catalysts prepared by MOF decomposition, Nanoscale 12(29) (2020) 15800-15813.
[42] M. Görlin, J. Halldin Stenlid, S. Koroidov, H.-Y. Wang, M. Börner, M. Shipilin, A. Kalinko, V. Murzin, O.V. Safonova, M. Nachtegaal, A. Uheida, J. Dutta, M. Bauer, A. Nilsson, O. Diaz-Morales, Key activity descriptors of nickel-iron oxygen evolution electrocatalysts in the presence of alkali metal cations, Nature Communications 11(1) (2020) 6181.
[43] R. Arrigo, S. Gallarati, M.E. Schuster, J.M. Seymour, D. Gianolio, I. Silva, J. Callison, H. Feng, J.E. Proctor, P. Ferrer, F. Venturini, D. Grinter, G. Held, Influence of Synthesis Conditions on the Structure of Nickel Nanoparticles and their Reactivity in Selective Asymmetric Hydrogenation, ChemCatChem 12(5) (2020) 1491-1503.
[44] Tarachand, V. Sharma, J. Singh, C. Nayak, D. Bhattacharyya, N. Kaurav, S.N. Jha, G.S. Okram, Size-Induced Structural Phase Transition at ~6.0 nm from Mixed fcc–hcp to Purely fcc Structure in Monodispersed Nickel Nanoparticles, The Journal of Physical Chemistry C 120(49) (2016) 28354-28362.
[45] M. Ushiro, K. Uno, T. Fujikawa, Y. Sato, K. Tohji, F. Watari, W.-J. Chun, Y. Koike, K. Asakura, X-ray absorption fine structure (XAFS) analyses of Ni species trapped in graphene sheet of carbon nanofibers, Physical Review B 73(14) (2006) 144103.

[46] Y. Li, Z.-S. Wu, P. Lu, X. Wang, W. Liu, Z. Liu, J. Ma, W. Ren, Z. Jiang, X. Bao, High-Valence Nickel Single-Atom Catalysts Coordinated to Oxygen Sites for Extraordinarily Activating Oxygen Evolution Reaction, Advanced Science 7(5) (2020) 1903089.
[47] R. Walczak, A. Savateev, J. Heske, N.V. Tarakina, S. Sahoo, J.D. Epping, T.D. Kühne, B. Kurpil, M. Antonietti, M. Oschatz, Controlling the strength of interaction between carbon dioxide and nitrogen-rich carbon materials by molecular design, Sustainable Energy & Fuels 3(10) (2019) 2819-2827.
[48] X. Li, L. Zhu, Q. Xue, X. Chang, C. Ling, W. Xing, Superior Selective CO2 Adsorption of C3N Pores: GCMC and DFT Simulations, ACS Applied Materials & Interfaces 9(36) (2017) 31161-31169.
[49] H. Yang, Q. Lin, C. Zhang, X. Yu, Z. Cheng, G. Li, Q. Hu, X. Ren, Q. Zhang, J. Liu, C. He, Carbon dioxide electroreduction on single-atom nickel decorated carbon membranes with industry compatible current densities, Nat Commun 11(1) (2020) 593.
[50] T. Zheng, K. Jiang, N. Ta, Y. Hu, J. Zeng, J. Liu, H. Wang, Large-Scale and Highly Selective CO2 Electrocatalytic Reduction on Nickel Single-Atom Catalyst, Joule 3(1) (2019) 265-278.
[51] Y. Cheng, S. Zhao, B. Johannessen, J.-P. Veder, M. Saunders, M.R. Rowles, M. Cheng, C. Liu, M.F. Chisholm, R. De Marco, H.-M. Cheng, S.-Z. Yang, S.P. Jiang, Atomically Dispersed Transition Metals on Carbon Nanotubes with Ultrahigh Loading for Selective Electrochemical Carbon Dioxide Reduction, Advanced Materials 30(13) (2018) 1706287.
[52] H.B. Yang, S.-F. Hung, S. Liu, K. Yuan, S. Miao, L. Zhang, X. Huang, H.-Y. Wang, W. Cai, R. Chen, J. Gao, X. Yang, W. Chen, Y. Huang, H.M. Chen, C.M. Li, T. Zhang, B. Liu, Atomically dispersed Ni(i) as the active site for electrochemical CO2 reduction, Nature Energy 3(2) (2018) 140-147.
[53] K. Jiang, S. Siahrostami, T. Zheng, Y. Hu, S. Hwang, E. Stavitski, Y. Peng, J. Dynes, M. Gangisetty, D. Su, K. Attenkofer, H. Wang, Isolated Ni single atoms in graphene nanosheets for high-performance CO2 reduction, Energy & Environmental Science 11(4) (2018) 893-903.
[54] P. Lu, Y. Yang, J. Yao, M. Wang, S. Dipazir, M. Yuan, J. Zhang, X. Wang, Z. Xie, G. Zhang, Facile synthesis of single-nickel-atomic dispersed N-doped carbon framework for efficient electrochemical CO2 reduction, Applied Catalysis B: Environmental 241 (2019) 113-119.
[55] L. Sun, V. Reddu, A.C. Fisher, X. Wang, Electrocatalytic reduction of carbon dioxide: opportunities with heterogeneous molecular catalysts, Energy & Environmental Science 13(2) (2020) 374-403.
[56] J.E. Pander, D. Ren, Y. Huang, N.W.X. Loo, S.H.L. Hong, B.S. Yeo, Understanding the Heterogeneous Electrocatalytic Reduction of Carbon Dioxide on Oxide-Derived Catalysts, ChemElectroChem 5(2) (2018) 219-237.
[57] L.F. Huang, M.J. Hutchison, R.J. Santucci, J.R. Scully, J.M. Rondinelli, Improved Electrochemical Phase Diagrams from Theory and Experiment: The Ni–Water System and Its Complex Compounds, The Journal of Physical Chemistry C 121(18) (2017) 9782-9789.
[58] m.a.v.m.s.f.s.m.a.B. II, mySpot: a versatile microfocussing station for scanning methods at BESSY II, Journal of large-scale research facilities JLSRF 2 (2016).
[59] T.m.b.a.B. II, The mySpot beamline at BESSY II, Journal of large-scale research facilities JLSRF 2 (2016).
[60] B. Ravel, M. Newville, ATHENA, ARTEMIS, HEPHAESTUS: data analysis for X-ray absorption spectroscopy using IFEFFIT, Journal of Synchrotron Radiation 12(4) (2005) 537-541.
[61] B.G. Lippert, J.H. Parrinello, Michele, A hybrid Gaussian and plane wave density functional scheme, Molecular Physics 92(3) (1997) 477-488.

[62] T.D. Kühne, M. Iannuzzi, M.D. Ben, V.V. Rybkin, P. Seewald, F. Stein, T. Laino, R.Z. Khaliullin, O. Schütt, F. Schiffmann, D. Golze, J. Wilhelm, S. Chulkov, M.H. Bani-Hashemian, V. Weber, U. Borštnik, M. Taillefumier, A.S. Jakobovits, A. Lazzaro, H. Pabst, T. Müller, R. Schade, M. Guidon, S. Andermatt, N. Holmberg, G.K. Schenter, A. Hehn, A. Bussy, F. Belleflamme, G. Tabacchi, A. Glöß, M. Lass, I. Bethune, C.J. Mundy, C. Plessl, M. Watkins, J. VandeVondele, M. Krack, J. Hutter, CP2K: An electronic structure and molecular dynamics software package - Quickstep: Efficient and accurate electronic structure calculations, The Journal of Chemical Physics 152(19) (2020) 194103.
[63] J. VandeVondele, J. Hutter, Gaussian basis sets for accurate calculations on molecular systems in gas and condensed phases, The Journal of Chemical Physics 127(11) (2007) 114105.
[64] E. Perlt, P. Ray, A. Hansen, F. Malberg, S. Grimme, B. Kirchner, Finding the best density functional approximation to describe interaction energies and structures of ionic liquids in molecular dynamics studies, The Journal of Chemical Physics 148(19) (2018) 193835.
[65] S. Goedecker, M. Teter, J. Hutter, Separable dual-space Gaussian pseudopotentials, Physical Review B 54(3) (1996) 1703-1710.
[66] T.D. Kühne, M. Krack, F.R. Mohamed, M. Parrinello, Efficient and Accurate Car-Parrinello-like Approach to Born-Oppenheimer Molecular Dynamics, Phys. Rev. Lett. 98(6) (2007) 066401.
[67] T.D. Kühne, Second generation Car–Parrinello molecular dynamics, WIREs Computational Molecular Science 4(4) (2014) 391-406.
[68] T.D. Kühne, E. Prodan, Disordered crystals from first principles I: Quantifying the configuration space, Annals of Physics 391 (2018) 120-149.
[69] T.A. Manz, N.G. Limas, Introducing DDEC6 atomic population analysis: part 1. Charge partitioning theory and methodology, RSC Advances 6(53) (2016) 47771-47801.
[70] S. Grimme, C. Bannwarth, P. Shushkov, A Robust and Accurate Tight-Binding Quantum Chemical Method for Structures, Vibrational Frequencies, and Noncovalent Interactions of Large Molecular Systems Parametrized for All spd-Block Elements (Z = 1–86), Journal of Chemical Theory and Computation 13(5) (2017) 1989-2009.

Biographies of authors

Enrico Lepre obtained his master's degree in chemistry at the University of Trieste focusing on nanomaterials and nanostructures for heterogeneous catalysis. He joined the colloid chemistry department of Max Planck Institute of Colloids and Interfaces (MPICI) to work on his Master thesis on synthetic strategies for carbocatalysts. After finishing his Master studies, he continued his research work at MPICI as a Ph.D. student. His current scientific interests are the design of carbonaceous materials as catalysts and support for third-period transition metal single-atom dispersions. His aim is to overcome the need for noble metals in heterogeneous catalysts.

Julian Heske is currently doing his PhD in theoretical chemistry as part of a collaboration between Prof. Thomas D. Kühne's research group at University of Paderborn (UPB) and Colloid Chemistry Departmetn at the MPICI. Previously, he received his B. Sc. and M. Sc. in chemistry at UPB. His current work is mainly focused on the computational investigation of novel carbon nitrides and related materials to understand their properties and promote their versatile applications.

Michal Nowakowski received his Ph.D. degree in physics at Institute of Nuclear Physics Polish Academy of Sciences in Krakow in 2019. Currently, he is a postdoctoral research fellow in the group of prof. Matthias Bauer in Paderborn University. He works in the field of static and ultrafast X-ray spectroscopies and their development and application to catalysis research.

Ernesto Scoppola obtained his Bachelor degree in 2009 and Master degree in 2012 at Tor Vergata University of Rome. His studies focused on neutron diffraction and Monte Carlo studies on glutathione water solutions. From 2012-2015, he did his PhD at the Institute Laue-Langevin in Grenoble and Montpellier University on liquid-liquid interfaces studied by x-ray and neutron reflectometry. In 2016, he joined Emanuel Schneck's group at the MPICI as a Postdoc were he investigated on bio-relevant soft interfaces. In 2020, he joined Wolfgang Wagermaier's group (MPICI) as instrument scientist on the μSpot CRG instrument at BESSY II (HZB). His current research interest focuses on SAXS tomography of bones.

Ivo Zizak got his PhD at the Montanistic University of Leoben, in 2000. After, he joined the former Hahn-Meitner-Institute, Berlin, Department for Structure and Dynamics of Materials, where he designed and built two experimental stations at the BESSY II synchrotron light source for surface and thin layers research. In 2007, he transferred to BESSY GmbH to build and operate several other X-ray beamlines. After, he joined the Department Structure and Dynamics of Energy Materials at HZB where he operates the micro-focusing experimental station at the mySpot beamline, where he develops combined scattering and XAS methods to study thin layers.

Tobias Heil started studying Physics in 2000 at the Westfälische Wilhelms-Universität Münster, Germany, where he finished his Diploma in 2006 and his PhD in 2010. From here, he moved to Liverpool, UK, to work as Research Associate at the Nanoinvestigation Centre of the University of Liverpool. In 2016, he went back to Germany, this time to Potsdam to take the position as Postdoc at the Max Planck Institute of Colloids and Interfaces. Since 2020, he works

as an engineer at the Stuttgart Center for Electron Microscopy of the Max Planck Institute for Solid State Research.

Thomas D. Kühne studied computer science (B. Sc. in 2003) and computational science and engineering (Dipl.-Rech. Wiss. in 2005) with a focus in theoretical chemistry at ETH Zürich. In 2008, he obtained his PhD from ETH Zürich in theoretical physics under the supervision of Prof. Michele Parrinello. After postdoctoral research on multiscale simulation methods within the theoretical condensed matter group at Harvard University, he joined the University of Mainz as an assistant professor in theoretical chemistry in 2010. In 2014 he joined UPB as a tenured associate professor in „Theoretical Interface Chemistry". In 2018, he was promoted to full professor and now holds the newly established Chair of Theoretical Chemistry.

Prof. Markus Antonietti received his Ph.D. from the University of Mainz in 1985. Prof. Antonietti is currently the Director of the Max Planck Institute of Colloids and Interfaces and has worked in the field of functional materials for 30 years. His current scientific interests include green chemistry and material solutions for the energy change, porous materials, artificial photosynthesis, and carbocatalysis, as well as the chemistry of cooking.

Nieves López-Salas received her Ph.D. from the Universidad Autonoma of Madrid in 2017. Her studies were carried out at the Bioinspired Group of the Institute of Materials Sciences of Madrid (ICMM-CSIC) under the tuition of Prof. Francisco del Monte. In 2018, she joined the Colloid Chemistry Department at the Max Planck Institute of Colloids and Interfaces where she works now as Group Leader. Her current research interests are the preparation of carbons at low temperature and noble carbonaceous materials and their use as carbocatalysts, gas sorbents and electrodes in energy conversion and storage devices.

Josep Albero was graduated in Chemical Engineering in the Jaume I University in 2005. He obtained his Ph. D. about the study of photo-induced charge transfer reactions in quantum dots based solar cells under the supervision of Prof. Palomares at ICIQ in 2012. He has conducted postdoctoral research in the Prof. Garcia group, at ITQ, and in Prof. Antonietti group, at MPIKG. His research interests include the preparation of advanced multifunctional materials and their application in the fields of energy conversion and storage. Dr. Albero is also interested in the study of the charge transfer reactions that limit the materials efficiency in these fields.

E. Lepre

N. López Salas

J. Albero

Oxygen coordinated nickel sites decorated over noble carbonaceous supports yield formic acid with 27% Faradaic efficiency when forming small clusters.

Enrico Lepre, Julian Heske, Michal Nowakowski, Ernesto Scoppola, Ivo Zizak, Tobias Heil, Thomas D. Kühne, Markus Antonietti, Nieves López-Salas* and Josep Albero*

Ni-Based Electrocatalysts for Unconventional CO_2 Reduction Reaction to Formic Acid